Journal of Materials Chemistry A

PAPER

Cite this: J. Mater. Chem. A, 2015, 3, 412

Observation of lithiation-induced structural variations in TiO_2 nanotube arrays by X-ray absorption fine structure†

Dongniu Wang,‡[ab] Lijia Liu,[c] Xueliang Sun*[a] and Tsun-Kong Sham*[b]

Received 17th September 2014
Accepted 23rd October 2014

DOI: 10.1039/c4ta04873c

www.rsc.org/MaterialsA

We report here a study of self-organized TiO_2 nanotube arrays both in the amorphous and anatase phases with superior electrochemical performance upon lithiation and delithiation. X-ray absorption fine structure (XAFS) study at the Ti K and L, O K and Li K edges has been conducted to track the behavior. Characteristic features for amorphous and anatase TiO_2 are identified. After lithiation, it is found that although no obvious variation of chemical states is apparent at the Ti K and L edges, charge transfer from Ti 3d to O 2p and also partial amorphization of anatase TiO_2 are evident from spectral intensities. The Li and O K edge XAFS show the successful intercalation of lithium and reveal the existence of a nearly linear "O–Li–O" arrangement in the lithiated TiO_2 nanotube. This study helps in understanding of the lithiation process in nanostructured TiO_2 anodes from a spectroscopic viewpoint.

Introduction

Nanostructured TiO_2 has been extensively studied and used in photodegradation devices,[1] energy-harvesting systems, such as dye-sensitized photovoltaic cells,[2,3] and energy storage systems such as electrochemical capacitors[4] and lithium-ion batteries.[5–8] Especially, TiO_2 excites great interest in the battery field due to its high working potential and superior stability, where efforts are being made to expand applications in heavy-duty systems such as electric and hybrid electric vehicles. In order to obtain cells with both high energy density and power density, great attention has been focused on exploring various TiO_2 nanostructures with different phases.[9–12] Furthermore, the geometry or configuration could also significantly affect the performance of TiO_2. Fang[13] *et al.* and Han[14] *et al.* demonstrate that one-dimensional self-assembled arrays still exhibit excellent electrochemical behaviors at high current and power densities up to 30 A g^{-1} and 10 C, respectively, which is ascribed to the reduced resistance between the electrode and current collectors and also the improved efficiency of electron transportation along one-dimensional channels.[13–17] Despite the superior electrochemical performance, gleaning a comprehensive understanding of the effect of intercalating lithium ions into TiO_2 frameworks upon alterations of their structures and chemical states, is of paramount significance for both understanding the mechanism and optimization of the engineering design.

Since the report by Whittingham *et al.*,[18] the insertion of lithium into a TiO_2 framework has been intensively studied in which lithiation was conducted both chemically using *n*-butyllithium and electrochemically.[7,19–23] Among various characterization techniques such as Raman, NMR,[21] and XRD,[24] X-ray absorption fine structure (XAFS) is arguably the most powerful tool for illustrating the local structural evolution of elements of interest upon lithiation. XAFS probes the modulation of core-level transitions (absorption coefficient) of an element of interest by its chemical environment in both the near-edge and extended regions of the absorption coefficient above the threshold – commonly known as X-ray absorption near-edge structure (XANES) and extended X-ray absorption fine structure (EXAFS), respectively. XANES is an element, local structure and bonding-specific method following the dipole selection rules. EXAFS arises from interference of the outgoing and back-scattered photoelectron waves at the absorbing atom and yields information about the local structure of atoms, such as the interatomic distance between the absorbing atom and its neighboring atoms (bond length), coordination number, and

[a]Department of Mechanical and Materials Engineering, University of Western Ontario, London, Ontario, N6A 5B9, Canada. E-mail: xsun@eng.uwo.ca; Tel: +1 5196612111 ext. 87759

[b]Department of Chemistry, University of Western Ontario, London, Ontario, N6A 5B7, Canada. E-mail: tsham@uwo.ca; Tel: +1 5196612111 ext. 86341

[c]Soochow-Western Center for Synchrotron Radiation Research, Soochow University, Institute of Functional Nano and Soft Materials, Soochow University, Suzhou, Jiangsu, 215123, China

† Electronic supplementary information (ESI) available: EDS spectrum of amorphous TiO_2 nanotube, 2-D display of excitation energy across the Ti $L_{3,2}$ edge and O K edge (*y*-axis) *vs.* fluorescence/scattered X-ray energy (*x*-axis) from Ti and O detected with a silicon drift detector, O K edge XANES of Li_2CO_3 powder, FLY spectrum of amorphous TiO_2 rooted on Ti foil and first-derivative spectra of Ti K-edge XAFS for amorphous and anatase TiO_2, both before and after lithiation. See DOI: 10.1039/c4ta04873c

‡ Current address: Canadian Light Source Inc. 44 Innovation Boulevard, Saskatoon, Saskatchewan, S7N 2V3 Canada.

Debye–Waller factor (mean square deviation of the bond length) in the first several shells.[25–29]

With regard to the structure of lithiated phases of TiO_2 (Li_xTiO_2, $0 < x < 1$), extensive work has been conducted; for example, pioneering work from Ohzuku *et al.*[30] claimed the cubic $LiTiO_2$ phase while Bonino *et al.*[24] and Cava *et al.*[31] claimed the orthorhombic $Li_{0.5}TiO_2$ phase. Lafont *et al.*[23] performed an *in situ* study and found that anatase TiO_2 undergoes a two-stage transition: a *Imma* orthorhombic Li_xTiO_2 is first formed in a partially lithiated state followed by a cubic $LiTiO_2$ phase ($I4_1/amd$) in the fully lithiated state. More importantly, it should be noted that the stability and structure of Li_xTiO_2 are highly dependent on the pristine TiO_2 crystal phase (*e.g.* TiO_2–B,[32] ramsdellite[33,34] and anatase[35]) and the corresponding morphology (*e.g.* nanoparticles[19,23] and nanotubes[36]) of the TiO_2. Borghols *et al.*[37] conducted a Ti K-edge XAFS study on lithiated amorphous TiO_2 nanoparticles, where a pre-edge shift toward lower energy and a new shoulder are found after lithiation which are attributed to the oxygen vacancies. Similarly, Okumura *et al.*[32] also reported the t_{2g} peak shifted to lower energy in the Ti L_3-edge XANES spectra for submicrosized TiO_2–B. XAFS study of $Li_{2+x}Ti_3O_7$ ramsdellite[38] reveals that though the host lattice remains unchanged upon lithiation, the Ti K-edge EXAFS analysis reveals a slight interatomic distance alteration and a reduced number of unoccupied O 2p densities of states in the O K-edge XANES. Since nanostructured anodes[7,11,12,21,39,40] exhibit an improvement in the practical capacity approaching theoretical values and also high rate properties, it is crucial to gain additional insights to facilitate both fundamental and practical studies.

In this paper, we set up a protocol for high lithium-ion battery (LIB) performance tracked by XAFS. We first synthesized self-organized TiO_2 nanotube arrays both in amorphous and anatase phases on Ti foil using an electrochemical anodization method and then conducted the lithiation with the electrochemical behaviors evaluated. Finally, a detailed XAFS analysis was conducted to investigate the effect of lithium intercalation on the structure of TiO_2 from the Ti, O and Li perspective.

Experimental methods

TiO_2 NT

TiO_2 NT arrays were synthesized using a one-step anodization process by applying a DC (direct current) power supply with a voltage around 16 V. Ti foil (0.1 mm thick, Goodfellow Ltd.) and a Pt wire were used as anode and cathode, respectively. A glycerol-based electrolyte was used in which HF (0.5 wt%) and glycerol were mixed in a volumetric ratio of 1 : 9. To facilitate the growth of nanotubes with smooth walls, a small amount of H_2O (~250 μL) was added to the final mixture. Detailed procedures can be found in previously reported results.[41] After 6 hours, the self-organized TiO_2 nanotube was formed aligning vertically onto the Ti foil substrate. Then, the nanotubes were washed several times with deionized water and dried under a N_2 flow. In order to obtain a pure anatase phase,[41] the as-prepared TiO_2 nanotubes were annealed at 550 °C for 2 h, during which TiO_2 was fully crystallized into anatase.

Characterization

Samples were characterized by X-ray diffraction (XRD, Rigaku RU-200BVH with a Co Kα source ($\lambda = 1.7892$ Å)), field emission scanning electron microscopy (FE-SEM, Hitachi 4800S), and energy dispersive spectroscopy (EDS). The XAFS experiments were performed at the Canadian Light Source (CLS) located at the University of Saskatchewan. The Ti $L_{3,2}$ and O K-edge XANES were measured at the undulator-based spherical grating monochromator (SGM) beamline,[42,43] the Ti K-edge EXAFS were obtained at the soft X-ray microcharacterization beamline (SXRMB),[44] and the Li K edges were conducted at the variable line spacing plane grating monochromator (VLS-PGM) beamline.[45] Spectra were normalized to the incident photon flux, which was recorded using a refreshed Au mesh or a Ni mesh.

Electrochemical measurement

The measurements were conducted using two-electrode cells. The as-obtained samples were cut into disks and dried at 80 °C under vacuum overnight to remove the adsorbed water and then directly used as the working electrode considering the good electronic conductivity of Ti foil. Coin cells (CR2032 type) were assembled using lithium metal foil as the counter electrode and polypropylene as the separator inside an argon-filled glove box. The electrolyte was 1 M $LiPF_6$ in ethylene carbonate/dimethyl carbonate solvent (EC/DMC, 1 : 1 in volume). The profiles of galvanostatic charging and discharging curves were obtained on a computer-controlled battery tester system (Arbin BT-2000) in a voltage range of 1 V to 3 V (*vs.* Li^+/Li) with a current density of 100 mA g^{-1}. The specific capacity is calculated based on the mass of TiO_2 NT, which was obtained by stripping the TiO_2 NT from the substrate using adhesive tape. The lithiated TiO_2 nanotubes samples were prepared by discharging the half cells to 1 V at 100 mA g^{-1} in the first cycle, and then were disassembled from the cell and washed thoroughly with ethanol and DMC.

Results and discussion

The phase composition and crystallinity of the prepared TiO_2 NT arrays are identified by XRD, as shown in Fig. 1a. The as-made TiO_2 NT is amorphous, exhibiting no peaks related to crystalline TiO_2. The three peaks that can be observed come from the Ti foil substrate. The zoomed-in spectrum displays one broad peak centered at 30°, demonstrating its amorphous nature. The EDS spectrum (Fig. S1†) for amorphous TiO_2 clearly shows the Ti and O characteristic fluorescence lines, further indicating the successful preparation of TiO_2. After annealing, typical peaks for tetragonal anatase TiO_2 can be identified at the (101), (004) and (200) planes (JCPDS no. 2-387), indicating a phase transformation to crystalline anatase TiO_2 had taken place. The typical anatase TiO_2 cell is shown in Fig. 1b.

The channels along the [001] direction are clearly observable from the top view in Fig. 1c. Intriguingly, for both amorphous and anatase TiO_2, after electrochemical lithiation, no lithium-related new phase can be identified from the XRD spectra, and the original phases are well maintained, indicating that the

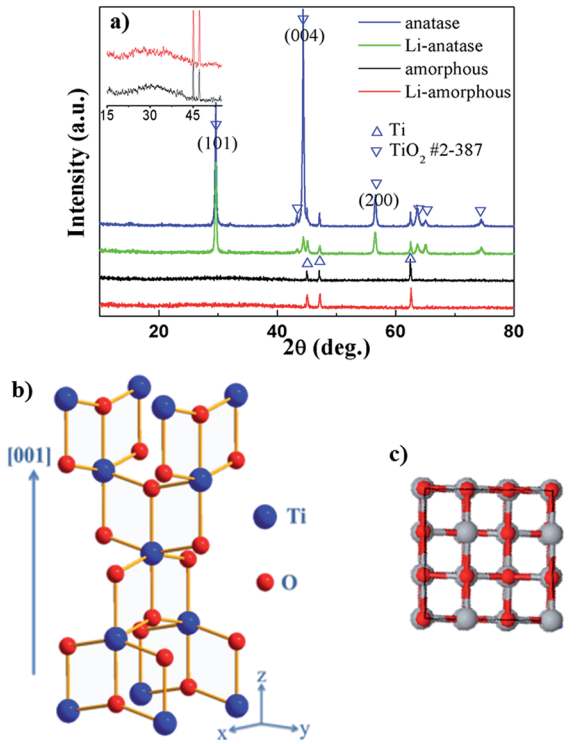

Fig. 1 (a) XRD spectra of the amorphous and anatase TiO_2 NT before and after lithiation, inset is the magnified spectra with angles between 15 and 45 degrees. (b) Scheme of the TiO_2 anatase unit cell. (c) Top view showing the channels along [001] (grey ball: Ti, red ball: O).

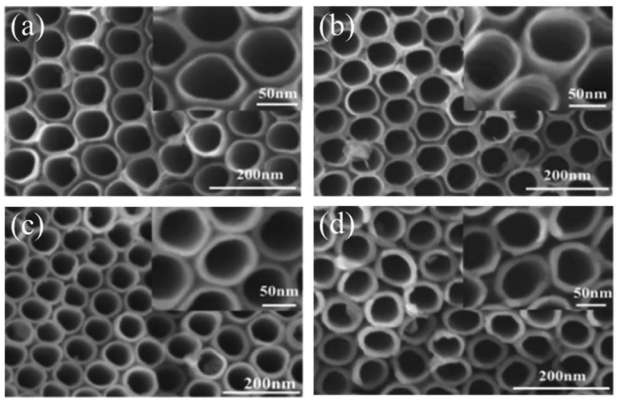

Fig. 2 SEM images of (a) amorphous TiO_2 NT; (b) lithiated amorphous TiO_2 NT; (c) anatase TiO_2 NT; (d) lithiated anatase TiO_2 NT (insets show magnified views of the TiO_2 NTs).

lithiation process does not change the phase composition markedly. For anatase TiO_2, the (004) plane before lithiation exhibits usually high intensity compared to other planes, illustrating that the well crystallographically oriented TiO_2 NT arrays are along the [001] direction.[46] It is noted, however, that the intensity of the (004) diffraction decreases drastically after lithiation, indicating a distortion of the TiO_2 plane after the introduction of lithium, which preferentially interacts with TiO_2 along the [001] direction and locates in between (004) planes. It has been reported that the (004) plane has higher surface energy compared to other planes (*e.g.* the (101) plane) which may facilitate the integration of lithium ions.[47] Since the lithiation process of TiO_2-based anodes is intercalation in nature, the introduction of lithium into TiO_2 does not significantly alter the integrity of the framework, as shown by the similar intensities and widths of other peaks of the lithiated TiO_2 compared to those of TiO_2 before lithiation.

SEM images of TiO_2 NT arrays both before and after lithiation are shown in Fig. 2. Similar to our previous results, the amorphous (Fig. 2a) and anatase NT (Fig. 2c) grow vertically on the Ti foils with an outer diameter of ~70 nm. The length is around 400 nm depending on the reaction time.[41] After calcination, the wall thickness increases slightly, leading to a smaller inner diameter for anatase TiO_2 compared with that of amorphous TiO_2. The morphologies of the samples after lithiation are also examined, as shown in Fig. 2b and d. It is found that for both amorphous and anatase TiO_2, the morphologies remain intact after cycling. This observation is in good accord with results reported by Fang *et al.*[13] It should be noted that the volume variation upon lithiation for TiO_2 is quite small (around 3%), and that a large surface to volume ratio and the presence of voids in nanotubes help accommodate the stress and strain. As a result, the lithiation process has little effect on the morphology of the aligned nanotubes.

The electrochemical performances of the TiO_2 NT specimens are further examined and the results are shown in Fig. 3. The initial discharge and charge profiles for amorphous and anatase TiO_2 NT are presented in Fig. 3a and b, respectively. From stage A to B, the NTs are discharged and insertion of lithium ions into TiO_2 occurs. In the charge process, the lithium ions are extracted from the TiO_2 framework and stage C is reached. Obviously, amorphous and anatase TiO_2 NT exhibit different voltage plateaus. For anatase TiO_2, it presents discharge and charge plateaus at around 1.7 V and 1.9 V, respectively, corresponding to the insertion and extraction of lithium ions, while the as-made TiO_2, due to the large amount of defects and the disordered structure, shows an expanded potential range. As a result, the curves show no obvious potential plateaus. The shapes of the curves are in good agreement with the earlier reports on amorphous and anatase TiO_2.[12,13,48,49] The amorphous TiO_2 NT delivers an initial discharge capacity of 311 mA h g^{-1} and a charge capacity of 259 mA h g^{-1} with a coulombic efficiency of 83%. The anatase TiO_2 NT delivers first discharge and charge capacities of 201 and 180 mA h g^{-1}, respectively. The initial coulombic efficiency is 90%. It is conceivable that the defect-rich and disordered structure in amorphous TiO_2 NT could supply more space for the insertion of lithium ions, leading to a higher capacity compared with that for anatase TiO_2. The cycling behaviors for TiO_2 NTs are shown in Fig. 3c. It is concluded that both amorphous and anatase TiO_2 exhibit quite stable retention of capacity in the first 10 cycles after the initial decay of the capacity, which is due to irreversible solid electrolyte interphase formation.

A higher irreversible capacity in amorphous TiO_2 NT may be due to more trapped lithium ions inside the titanate framework at defect sites[13,50] and a higher amount of solid-electrolyte

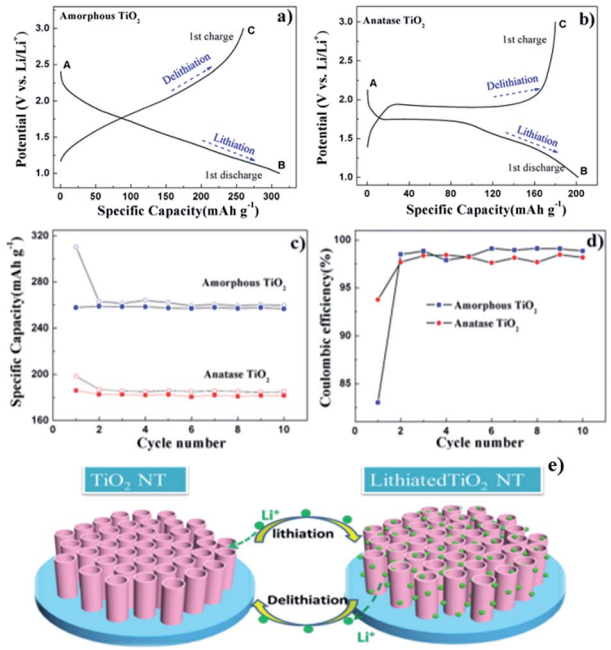

Fig. 3 Initial charge–discharge profiles of (a) amorphous TiO_2 and (b) anatase TiO_2 at 100 mA g^{-1} (A, B and C represent different stages for lithiation and delithiation); (c) cycling behavior of amorphous and anatase TiO_2 in the first 10 cycles at 100 mA g^{-1} in the voltage window of 1.0 V to 3.0 V (hollow dots: discharge curves; solid dots: charge curves); (d) comparison of coulombic efficiency of amorphous TiO_2 and anatase TiO_2 in the first 10 cycles; (e) schematic representation of lithiation process in TiO_2 nanotube arrays.

interface (SEI) layers formed in the thinner tube walls compared to that of anatase. After 10 cycles, the discharge capacities for amorphous TiO_2 and anatase TiO_2 are stabilized at 260 mA h g^{-1} and 185 mA h g^{-1}, respectively. As shown in Fig. 3c and d, the cycling curves become flat and the coulombic efficiencies of both samples remain around 97% starting from the second cycle, indicating superior cycling performance. The stable cyclability for both NT should be ascribed to the intrinsic small volume variation and also the one-dimensional nanotube morphology, which accommodate the stress and maintain the original structure very well. As demonstrated in Fig. 3e, upon cycling, lithium ions are reversibly intercalated into and deintercalated from the self-organized TiO_2 nanotube arrays, where the structure and morphologies are essentially intact.

Ti $L_{3,2}$-edge and O K-edge XANES

To characterize the electronic structure and local structure of the TiO_2 NT before and after lithiation, XANES at the Ti $L_{3,2}$ edge and the O K edge have been obtained using partial, element-specific X-ray fluorescence yield monitored with an energy-dispersive silicon drift detector (SDD), which generates a color-coded 2D display of excitation energy *versus* X-ray fluorescence energy.[51] Fig. S2† shows the 2D display of excitation energy across the Ti $L_{3,2}$ and O K edge *versus* X-ray fluorescence energy recorded by a silicon drift detector (SDD) with the relative intensity color bar as shown in the image. The Ti $L_{3,2}$ and O K-edge XANES spectra are obtained by monitoring the response of the corresponding fluorescence (dashed lines) as a function of the excitation energy. There is clearly sufficient energy resolution separating the Ti Lα (452.2 eV) and O Kα (524.9 eV) fluorescence lines.

Fig. 4 shows the Ti $L_{3,2}$-edge XANES spectra for amorphous and anatase TiO_2 NT, henceforth denoted AM–TiO_2 and AN–TiO_2 respectively, both before and after lithiation. The features of interest are marked by vertical dashed lines. Typical features arising from the transitions of Ti 2p electrons to previously unoccupied 3d electronic states in a distorted octahedral crystal field can be clearly identified. A weak shoulder doublet in all the compounds, denoted a and b, is related to transitions which are dipole-forbidden, but are possible due to multiple interaction.[52] Peaks c and f are ascribed to the transition from $2p_{3/2}$ and $2p_{1/2}$ to t_{2g}, respectively, while d, e and g are attributed to the transition from $2p_{1/2}$ to e_g.[36,41,53,54] It is interesting to note that the relative intensity of d and e is reversed in rutile TiO_2 and in $SrTiO_3$, where Ti is in a perfect octahedral environment, there is no splitting and d and e merge into a single peak. It is apparent the d, e doublet in Fig. 4a is anatase-like and more pronounced while it is blurred in amorphous TiO_2 NT. Since e_g states are sensitive to the variation in symmetry, the further splitting in spectra at e_g states of the L_3 edge for anatase TiO_2 should be attributed to the distortion to D_{2d}.[52,54] Since as-made TiO_2 is amorphous and shows a lack of long-range ordering, the local distortion of Ti is an average of all arrangements, leading to the broadening of the e_g peak.

Turning to the spectra for lithiated samples, it is apparent that the spectra are quite similar to those before lithiation, indicating that the local environment and the electronic structure of Ti are well maintained after the introduction of lithium ions. Since the volume variation for TiO_2 is quite small and it is a tubal structure, the original local structures of the Ti–O framework are well retained after lithiation. Closer observation reveals a broadening feature at the e_g states (d and e) and also the pre-edges (a and b) for the lithiated anatase TiO_2 nanotube, which could be attributed to a slight amorphization or distortion of the crystalline TiO_2 framework by lithium ions as demonstrated from the XRD spectra where the (004) diffraction intensity is greatly reduced. It is conceivable that the lithium ions lie in the [001] direction of the TiO_2 framework along the

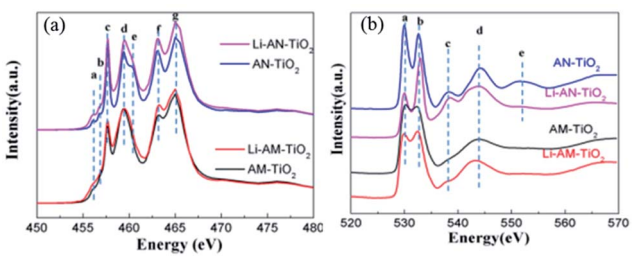

Fig. 4 (a) Ti $L_{3,2}$-edge XANES and (b) O K-edge XANES of amorphous TiO_2 NT, anatase TiO_2 NT, lithiated amorphous and anatase TiO_2 NT obtained at stage B in Fig. 3 (AM–TiO_2: amorphous TiO_2; AN–TiO_2: anatase TiO_2).

channels shown in Fig. 1c. These are different from the results reported by Okumura *et al.*,[32] where they claimed a Ti^{4+} to Ti^{3+} transition upon lithiation at the Ti L edge in a submicrosized TiO_2–B phase. More importantly, they further compared it with TiO_2–B nanowires of different size.[55] After lithiation, it is found that the Ti K-edge XAFS spectra of Li_xTiO_2–B nanowires remain unchanged, indicating that the local structural change for Ti is limited in nanoparticles without chemical states variation. Here, for TiO_2 nanotube arrays, no detectable shift of the absorption peaks at the Ti $L_{3,2}$ edge is found, indicating that lithium insertion does not lead to a local valence variation of Ti similar to the nanowires reported by Okumura *et al.*,[55] instead, it may only change the interaction (*e.g.* covalency or ionicity) between Ti and O ions analogous to that reported by Zhou *et al.* previously.[36] Also, a slight increase in intensity of the white line is evident for both lithiated amorphous and anatase TiO_2 at the $L_{3,2}$ edge, indicating either electron depletion at the Ti 3d projected orbital, or transition matrix element effects due to the lithium intercalation, or both.

Fig. 4b shows the transitions of O 1s to unoccupied 2p states in the conduction band. The hybridization of Ti 3d and also 4s and 4p with O 2p determines the spectral features. The first two sharp peaks for a and b arise from hybridization with Ti 3d states while the following peaks are ascribed to the O 2p antibonding state and hybridization with s and p states of Ti.[41,53,56] Crystalline anatase TiO_2 shows characteristic features similar to previously reported results,[57] while amorphous TiO_2 NT exhibits broadened and smoothed-out features, for example, the loss of resonance e due to its low crystallinity and lack of long-range order. However, the locally ordered features could still be tracked, such as peaks a, b and d, similar to those in the Ti $L_{3,2}$-edge XANES. The intensity ratio of peaks c to d in the Ti L-edge XANES of AM–TiO_2 is also lower compared with that of anatase, indicating a weaker crystal field or more under-coordinated Ti atoms.[58]

For the lithiated sample, we see that for the amorphous TiO_2 the spectrum matched well with that of TiO_2 before lithiation, indicating a well-maintained local environment for O. The defects and disordered structure in amorphous TiO_2 may help supply extra space to accommodate lithium ions, resulting in little significant influence on the local chemistry for O atoms. However, closer examination indicates a slight increase in the peak intensity ratio of b to a and a slight energy shift of peak a toward lower energy upon lithiation. For the lithiated anatase TiO_2, the peak intensity ratio of b to a increases significantly with a more pronounced feature at peak c and a smoothed-out feature at e. A similar trend, albeit less noticeable, is also found in the amorphous TiO_2 group. A closer look reveals a noticeably weaker resonance at peak a for lithiated anatase TiO_2. Peak a arises from the transition from O 1s to O 2p states which are hybridized with Ti t_{2g} states, while peak b refers to resonance to 2p states hybridized with Ti e_g states. We also examine the O K-edge XANES of Li_2CO_3, which is a common by-product during charging and discharging in a carbonate-based electrolyte, as shown in Fig. S3.† It exhibits a sharp edge jump at around 539 eV which is assigned to the 1s electrons to the π^* (C=O) orbitals, similar to that reported by Yang *et al.*[59] Further examination shows no resonances at a (530 eV) or b (532.6 eV) in the O K-edge XANES of Li_2CO_3; thus the suppressed transition at peak a should be exclusively attributed to the lithiated TiO_2, indicating increased occupation of hybrid t_{2g} states and a charge transfer to 2p states of O character. Since lithium ions are trapped in the crystalline TiO_2 framework, the highly electropositive lithium ions may induce the charge relocation to the O 2p-Ti t_{2g} bands without affecting the local symmetry significantly. Okumura *et al.*[55] also found a similar electron injection into the unoccupied O 2p orbital after lithiation for TiO_2–B nanowires. Furthermore, the enhanced transition at peak c indicates an increment corresponding to the antibonding O 2p transition, which may be caused by the nearly linear O–Li–O arrangement where Li lies in the outgoing path of the O photoelectron wave.[36,60] Finally, the smoothed-out feature e may be due to the lack of long-range ordering and slight amorphization, similar to the lack of splitting at e_g states observed at the Ti L_3 edge.

Li K-edge XANES

Fig. 5a shows the Li K-edge XANES of TiO_2 samples after initial lithiation and 10 cycles. The spectrum for Li_2CO_3 is also provided, which is a common component of a solid-electrolyte interphase in a carbonate-based electrolyte. Lithiated amorphous and anatase TiO_2 nanotubes show similar resonance. The intense transitions at 62 eV and 67.2 eV should be attributable to the multiple scattering of the p wave by the cage environment,[51] while the edge jump at about 60 eV is highly suppressed in all samples, illustrating a more covalent feature for lithium ions and surrounding atoms. Similar to Li K-edge XANES for $LiCoO_2$ as reported by Zhou *et al.*,[36] where Li ions are also intercalated into the framework, the lithiated TiO_2 NT presents similar resonances with the main edge jump occurring at 62 eV. Upon further comparison of the XANES spectra, it is found that the Li_2CO_3 are formed after cycling. For Li–AN–TiO_2, after the initial lithiation process, the Li_2CO_3 is already formed as can be seen from the shoulder shown in peak e of the spectrum. Since a one-dimensional NT has a large surface to volume ratio, many sites are available for Li_2CO_3 to deposit and coexist

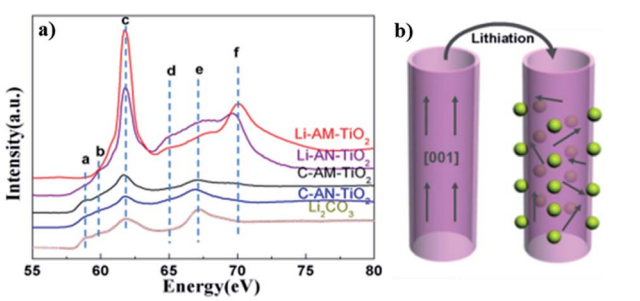

Fig. 5 (a) Li K-edge XANES for lithiated TiO_2 samples at stage B in Fig. 3 (denoted as Li–AM–TiO_2 and Li–AN–TiO_2), the samples after 10 discharge–charge cycles (denoted as C–AM–TiO_2 and C–AN–TiO_2) and standard Li_2CO_3. (b) Schematic diagrams show process of the lithium-driven random orientation for anatase TiO_2 NT. Yellow dots stand for lithium ions which arrange along [001].

with lithiated TiO_2. After 10 cycles of discharge and charge, Li ions are extracted from the TiO_2 framework, while the stable Li_2CO_3 is left behind, thus C–AN–TiO_2 presents distinct resonance features originating from Li_2CO_3, as shown in the first weak shoulder doublet (peaks a and b) and also the edge jump at peaks c and e. A similar trend could also be found in the amorphous TiO_2 group, where more significant features of Li_2CO_3 appeared after 10 cycles. Although it is still unclear what the resonance at 70 eV is, based on the above discussion of Ti L and O K-edge XANES, it most probably arises from the lithiated TiO_2, possibly a multiple scattering between Li and surrounding atoms in the lithiated TiO_2 framework. Fig. 5b shows schematic diagrams of anatase TiO_2 NT upon lithiation. During intercalation, lithium ions locate themselves along the [001] direction forming a nearly linear "O–Li–O" bond in the tubes, while the orientation for highly ordered anatase TiO_2 NT becomes distorted. Thus Li K-edge XANES successfully tracks the intercalation of lithium into the TiO_2 framework and reveals the local structures for Li atoms.

Ti K-edge XAFS

Ti K-edge XAFS is also informative about the local structure around Ti atoms, as shown in Fig. 6. The fluorescence yield (FLY) spectrum recorded for the amorphous TiO_2 sample (Fig. S4†) presents a spectrum feature similar to Ti(0) rather than TiO_2. As we know, the penetration depth for X-rays at the Ti K edge is around 20 μm based on calculations from an X-ray calculator;[61] since the TiO_2 arrays have a thickness of 400 nm, thus a FLY spectrum could unveil information coming from the Ti foil underneath. A surface-sensitive total electron yield spectrum is thus used here for TiO_2. Fig. 6a shows the XANES spectra of the pristine and lithiated TiO_2 samples. All the spectra present typical pre-edge features and the white line. For anatase TiO_2, the pre-edge features are marked a, b and c, which arise from hybridization of p and d orbitals of the Ti atom and surrounding neighbors.[62–65] Peak a is attributed to the quadrupole transition of 1s to t_{2g} states of octahedral TiO_6,[66–69] while peak b and c assignments are controversial – resonance b is either attributed to the 1s to e_g transition of octahedral TiO_6 or the transition to t_{2g} of neighboring octahedra.[67–69] Peak c is attributed to the transition to e_g states of neighboring Ti atoms or 4p states of absorbing atoms.

The weak shoulder between c and d stands for the 1s to 4p transition, while peak d is the higher-lying p atomic orbitals.[66,70–73] It is further identified that anatase TiO_2 exhibits well-resolved peaks and sharp features at e and f due to its high crystallinity. In contrast, the amorphous TiO_2 is broader with blurred features. The intense single pre-edge peak suggests Ti-oxide species exist in tetrahedral or pentahedral coordination.[57,74] For poorly crystalline TiO_2, a distorted or defective Ti environment is expected, leading to increased distortion and thus increased resonance intensity at the pre-edge. Similar to Ti L-edge XANES, the spectrum for lithiated samples is nearly the same as the pristine samples, indicating that the TiO_2 framework is well retained after lithiation due to the low volume variation and also the one-dimensional tubal NT structure. The first derivative of XANES spectra shown in Fig. S5† for a lithiated TiO_2 nanotube is almost the same as the pristine ones without an energy shift, further demonstrating that the chemical states are stable for Ti ions upon lithiation.

Fourier transformations (FT) of the EXAFS spectra[75] are shown in Fig. 6b and c. The FTs for the two phases of TiO_2 exhibit distinct different characteristic features as shown in Fig. S6.† The coordination change can be clearly observed in the EXAFS region (in *k*-space). For FT-EXAFS in Fig. 6b, A, B, and C stand for the Ti–O, Ti–Ti and Ti–O–Ti coordination shells, respectively.[76,77] The existence of peak C indicates high crystallinity.[78] For amorphous TiO_2, the Fourier transformation of EXAFS spectra is quite different, while the Ti–O, Ti–Ti and Ti–O–Ti bonds could still be tracked as shown in Fig. 6c. The one major intense peak at shorter interatomic distance, centered at 1 Å, is too short even after a phase correction of ~0.4 Å to be a real bond distance; it most likely arises from a combination of high *k*-noise, the isolated Ti-oxide species of amorphous TiO_2 in tetrahedral or pentahedral coordination and the focusing effect of intervening Li in a chemically inhomogeneous Ti local environment. Turning to the spectra for the lithiated samples, we find that both of them exhibit similar EXAFS oscillations in the low *k*-region compared to pristine samples but with noticeable lower magnitudes and broadening, illustrating a lower coordination number on average of Ti atoms and hence an increase of disorder among them (larger static Debye–Waller factor). It should be noted that a similar feature at position D (around 1 Å in FT) for Li–AN–TiO_2 emerged after the lithiation process, which is similar to that for the amorphous TiO_2. The presence of Li can act as an electron lens modifying the EXAFS with enhanced intensity in the FT. It is concluded that for anatase TiO_2, lithiation of the TiO_2 leads to at least partial amorphization of the pristine TiO_2 which is in agreement with the Ti L-edge XANES.

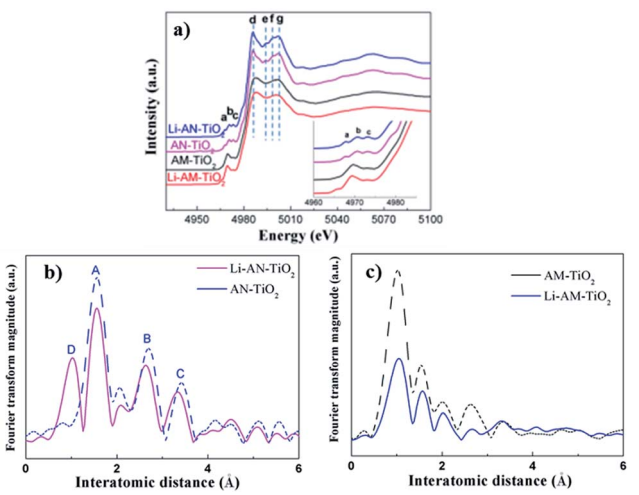

Fig. 6 (a) XANES of Ti K edge and (b), (c) Fourier-transformed (FT) Ti K-edge k^3-weighted EXAFS spectra for amorphous and anatase TiO_2, both before and after lithiation (*k*-range for the FT: 2.6–12.8 $Å^{-1}$). The inset of (a) shows the magnified pre-edge region.

Conclusions

Amorphous and anatase TiO_2 NT self-organized arrays have been successfully prepared and their lithium-ion storage capabilities are examined. Both of the TiO_2 NTs exhibit stable cycling performances benefiting from the 1D nanostructure and also the inherent low volume variation. Amorphous TiO_2 NTs exhibit higher capacity than anatase TiO_2 NTs due to their higher number of intercalation sites for lithium ions from the disordered structure. A detailed XAFS analysis has been conducted on the pristine and lithiated TiO_2 at the Ti L and K and O K edges. XAFS reveals different local symmetry, distortion and crystallinity in amorphous and anatase TiO_2. Li K-edge XANES confirms the introduction of Li into the TiO_2 framework, locating along the [001] direction of the TiO_2 framework, and its presence induces charge relocation to the O 2p-Ti t_{2g} bands as demonstrated from the O K-edge XANES. XANES and EXAFS spectra also reveal slight lithiation-induced amorphization of the TiO_2, while the chemical states of Ti and O are well maintained. This work demonstrates a case study of the effects of the lithiation process on structural variations in TiO_2 electrodes probed by the XAFS technique and could be easily extended to other electrodes and energy devices such as photovoltaic cells, capacitors and fuel cells.

Notes and references

1 R. Asahi, T. Morikawa, T. Ohwaki, K. Aoki and Y. Taga, *Science*, 2001, **293**, 269–271.
2 M. Law, L. E. Greene, J. C. Johnson, R. Saykally and P. D. Yang, *Nat. Mater.*, 2005, **4**, 455–459.
3 B. Oregan and M. Gratzel, *Nature*, 1991, **353**, 737–740.
4 T. Brousse, R. Marchand, P. L. Taberna and P. Simon, *J. Power Sources*, 2006, **158**, 571–577.
5 A. S. Arico, P. Bruce, B. Scrosati, J. M. Tarascon and W. Van Schalkwijk, *Nat. Mater.*, 2005, **4**, 366–377.
6 A. R. Armstrong, G. Armstrong, J. Canales, R. Garcia and P. G. Bruce, *Adv. Mater.*, 2005, **17**, 862–865.
7 L. Kavan, M. Kalbac, M. Zukalova, I. Exnar, V. Lorenzen, R. Nesper and M. Graetzel, *Chem. Mater.*, 2004, **16**, 477–485.
8 S. Y. Huang, L. Kavan, I. Exnar and M. Gratzel, *J. Electrochem. Soc.*, 1995, **142**, L142–L144.
9 H. S. Zhou, D. L. Li, M. Hibino and I. Honma, *Angew. Chem., Int. Ed.*, 2005, **44**, 797–802.
10 Q. Wang, Z. H. Wen and J. H. Li, *Adv. Funct. Mater.*, 2006, **16**, 2141–2146.
11 Y. S. Hu, L. Kienle, Y. G. Guo and J. Maier, *Adv. Mater.*, 2006, **18**, 1421–1426.
12 Y. G. Guo, Y. S. Hu, W. Sigle and J. Maier, *Adv. Mater.*, 2007, **19**, 2087–2091.
13 H. T. Fang, M. Liu, D. W. Wang, T. Sun, D. S. Guan, F. Li, J. G. Zhou, T. K. Sham and H. M. Cheng, *Nanotechnology*, 2009, **20**, 225701.
14 H. Han, T. Song, E. K. Lee, A. Devadoss, Y. Jeon, J. Ha, Y. C. Chung, Y. M. Choi, Y. G. Jung and U. Paik, *ACS Nano*, 2012, **6**, 8308–8315.
15 S. W. Kim, T. H. Han, J. Kim, H. Gwon, H. S. Moon, S. W. Kang, S. O. Kim and K. Kang, *ACS Nano*, 2009, **3**, 1085–1090.
16 F. X. Wu, Z. X. Wang, X. H. Li and H. J. Guo, *J. Mater. Chem.*, 2011, **21**, 12675–12681.
17 J. M. Li, W. Wan, H. H. Zhou, J. J. Li and D. S. Xu, *Chem. Commun.*, 2011, **47**, 3439–3441.
18 M. S. Whittingham and M. B. Dines, *J. Electrochem. Soc.*, 1977, **124**, 1387–1388.
19 M. Wagemaker, W. J. H. Borghols and F. M. Mulder, *J. Am. Chem. Soc.*, 2007, **129**, 4323–4327.
20 M. Wagemaker, W. J. H. Borghols, E. R. H. van Eck, A. P. M. Kentgens, G. L. Kearley and F. M. Mulder, *Chem.–Eur. J.*, 2007, **13**, 2023–2028.
21 V. Luca, T. L. Hanley, N. K. Roberts and R. F. Howe, *Chem. Mater.*, 1999, **11**, 2089–2102.
22 G. Sudant, E. Baudrin, D. Larcher and J. M. Tarascon, *J. Mater. Chem.*, 2005, **15**, 1263–1269.
23 U. Lafont, D. Carta, G. Mountjoy, A. V. Chadwick and E. M. Kelder, *J. Phys. Chem. C*, 2010, **114**, 1372–1378.
24 F. Bonino, L. Busani, M. Lazzari, M. Manstretta, B. Rivolta and B. Scrosati, *J. Power Sources*, 1981, **6**, 261–270.
25 H. Ade and H. Stoll, *Nat. Mater.*, 2009, **8**, 281–290.
26 T. E. Westre, P. Kennepohl, J. G. DeWitt, B. Hedman, K. O. Hodgson and E. I. Solomon, *J. Am. Chem. Soc.*, 1997, **119**, 6297–6314.
27 D. N. Wang, J. L. Yang, X. F. Li, J. J. Wang, R. Y. Li, M. Cai, T. K. Sham and X. L. Sun, *Cryst. Growth Des.*, 2012, **12**, 397–402.
28 D. N. Wang, J. L. Yang, X. F. Li, D. S. Geng, R. Y. Li, M. Cai, T. K. Sham and X. L. Sun, *Energy Environ. Sci.*, 2013, **6**, 2900–2906.
29 D. N. Wang, X. F. Li, J. L. Yang, J. J. Wang, D. S. Geng, R. Y. Li, M. Cai, T. K. Sham and X. L. Sun, *Phys. Chem. Chem. Phys.*, 2013, **15**, 3535–3542.
30 T. Ohzuku, Z. Takehara and S. Yoshizawa, *Electrochim. Acta*, 1979, **24**, 219–222.
31 R. J. Cava, D. W. Murphy, S. Zahurak, A. Santoro and R. S. Roth, *J. Solid State Chem.*, 1984, **53**, 64–75.
32 T. Okumura, T. Fukutsuka, A. Yanagihara, Y. Orikasa, H. Arai, Z. Ogumi and Y. Uchimoto, *J. Mater. Chem.*, 2011, **21**, 15369–15377.
33 M. V. Koudriachova, *Chem. Phys. Lett.*, 2008, **458**, 108–112.
34 M. V. Koudriachova, *Phys. Chem. Chem. Phys.*, 2008, **10**, 5094–5098.
35 B. J. Morgan and G. W. Watson, *J. Phys. Chem. Lett.*, 2011, **2**, 1657–1661.
36 J. G. Zhou, H. T. Fang, J. M. Maley, M. W. Murphy, J. Y. P. Ko, J. N. Cutler, R. Sammynaiken, T. K. Sham, M. Liu and F. Li, *J. Mater. Chem.*, 2009, **19**, 6804–6809.
37 W. J. H. Borghols, D. Lutzenkirchen-Hecht, U. Haake, W. Chan, U. Lafont, E. M. Kelder, E. R. H. van Eck, A. P. M. Kentgens, F. M. Mulder and M. Wagemaker, *J. Electrochem. Soc.*, 2010, **157**, A582–A588.
38 W. Ra, M. Nakayama, W. Cho, M. Wakihara and Y. Uchimoto, *Phys. Chem. Chem. Phys.*, 2006, **8**, 882–889.

39 G. Armstrong, A. R. Armstrong, P. G. Bruce, P. Reale and B. Scrosati, *Adv. Mater.*, 2006, **18**, 2597–2600.

40 D. H. Wang, D. W. Choi, J. Li, Z. G. Yang, Z. M. Nie, R. Kou, D. H. Hu, C. M. Wang, L. V. Saraf, J. G. Zhang, I. A. Aksay and J. Liu, *ACS Nano*, 2009, **3**, 907–914.

41 L. J. Liu, J. Chan and T. K. Sham, *J. Phys. Chem. C*, 2010, **114**, 21353–21359.

42 T. Regier, J. Krochak, T. K. Sham, Y. F. Hu, J. Thompson and R. I. R. Blyth, *Nucl. Instrum. Methods Phys. Res., Sect. A*, 2007, **582**, 93–95.

43 T. Regier, J. Paulsen, G. Wright, I. Coulthard, K. Tan, T. K. Sham and R. I. R. Blyth, *AIP Conf. Proc.*, 2007, **879**, 473–476.

44 Y. F. Hu, I. Coulthard, D. Chevrier, G. Wright, R. Igarashi, A. Sitnikov, B. W. Yates, E. L. Hallin, T. K. Sham and R. Reininger, *Sri 2009: The 10th International Conference on Synchrotron Radiation Instrumentation*, 2010, **1234**, 343–346.

45 Y. F. Hu, L. Zuin, G. Wright, R. Igarashi, M. McKibben, T. Wilson, S. Y. Chen, T. Johnson, D. Maxwell, B. W. Yates, T. K. Sham and R. Reininger, *Rev. Sci. Instrum.*, 2007, **78**, 083109.

46 S. Lee, I. J. Park, D. H. Kim, W. M. Seong, D. W. Kim, G. S. Han, J. Y. Kim, H. S. Jung and K. S. Hong, *Energy Environ. Sci.*, 2012, **5**, 7989–7995.

47 H. T. Tung, J. M. Song, S. W. Feng, C. S. Kuo and I. G. Chen, *Phys. Chem. Chem. Phys.*, 2010, **12**, 740–744.

48 Q. L. Wu, J. C. Li, R. D. Deshpande, N. Subramanian, S. E. Rankin, F. Q. Yang and Y. T. Cheng, *J. Phys. Chem. C*, 2012, **116**, 18669–18677.

49 I. Moriguchi, R. Hidaka, H. Yamada, T. Kudo, H. Murakami and N. Nakashima, *Adv. Mater.*, 2006, **18**, 69–73.

50 Y. Y. Zhang, Y. X. Tang, S. Y. Yin, Z. Y. Zeng, H. Zhang, C. M. Li, Z. L. Dong, Z. Chen and X. D. Chen, *Nanoscale*, 2011, **3**, 4074–4077.

51 S. L. Yang, D. N. Wang, G. X. Liang, Y. M. Yiu, J. J. Wang, L. J. Liu, X. L. Sun and T. K. Sham, *Energy Environ. Sci.*, 2012, **5**, 7007–7016.

52 F. M. F. Degroot, M. O. Figueiredo, M. J. Basto, M. Abbate, H. Petersen and J. C. Fuggle, *Phys. Chem. Miner.*, 1992, **19**, 140–147.

53 L. A. Grunes, R. D. Leapman, C. N. Wilker, R. Hoffmann and A. B. Kunz, *Phys. Rev. B: Condens. Matter Mater. Phys.*, 1982, **25**, 7157–7173.

54 F. M. F. Degroot, J. C. Fuggle, B. T. Thole and G. A. Sawatzky, *Phys. Rev. B: Condens. Matter Mater. Phys.*, 1990, **41**, 928–937.

55 T. Okumura, T. Fukutsuka, A. Yanagihara, Y. Orikasa, H. Arai, Z. Ogumi and Y. Uchimoto, *Chem. Mater.*, 2011, **23**, 3636–3644.

56 R. Brydson, H. Sauer, W. Engel, J. M. Thomas, E. Zeitler, N. Kosugi and H. Kuroda, *J. Phys.: Condens. Matter*, 1989, **1**, 797–812.

57 S. J. Stewart, M. Fernandez-Garcia, C. Belver, B. S. Mun and F. G. Requejo, *J. Phys. Chem. B*, 2006, **110**, 16482–16486.

58 G. S. Henderson, X. Liu and M. E. Fleet, *Phys. Chem. Miner.*, 2002, **29**, 32–42.

59 R. M. Qiao, Y. D. Chuang, S. S. Yan and W. L. Yang, *PLoS One*, 2012, **7**, e49182.

60 M. V. Koudriachova, S. W. de Leeuw and N. M. Harrison, *Phys. Rev. B: Condens. Matter Mater. Phys.*, 2004, **69**, 054106.

61 B. L. Henke, E. M. Gullikson and J. C. Davis, *At. Data Nucl. Data Tables*, 1993, **55**, 349.

62 F. Farges, G. E. Brown and J. J. Rehr, *Phys. Rev. B: Condens. Matter Mater. Phys.*, 1997, **56**, 1809–1819.

63 V. Luca, S. Djajanti and R. F. Howe, *J. Phys. Chem. B*, 1998, **102**, 10650–10657.

64 L. X. Chen, T. Rajh, W. Jager, J. Nedeljkovic and M. C. Thurnauer, *J. Synchrotron Radiat.*, 1999, **6**, 445–447.

65 T. Rajh, J. M. Nedeljkovic, L. X. Chen, O. Poluektov and M. C. Thurnauer, *J. Phys. Chem. B*, 1999, **103**, 3515–3519.

66 Z. Y. Wu, G. Ouvrard, P. Gressier and C. R. Natoli, *Phys. Rev. B: Condens. Matter Mater. Phys.*, 1997, **55**, 10382–10391.

67 T. Uozumi, K. Okada, A. Kotani, O. Durmeyer, J. P. Kappler, E. Beaurepaire and J. C. Parlebas, *Europhys. Lett.*, 1992, **18**, 85–90.

68 M. A. Khan, A. Kotani and J. C. Parlebas, *J. Phys.: Condens. Matter*, 1991, **3**, 1763–1772.

69 K. Okada and A. Kotani, *J. Electron Spectrosc. Relat. Phenom.*, 1993, **62**, 131–140.

70 J. C. Parlebas, M. A. Khan, T. Uozumi, K. Okada and A. Kotani, *J. Electron Spectrosc. Relat. Phenom.*, 1995, **71**, 117–139.

71 L. Q. Wang, K. F. Ferris, A. N. Shultz, D. R. Baer and M. H. Engelhard, *Surf. Sci.*, 1997, **380**, 352–364.

72 F. Farges, G. E. Brown and J. J. Rehr, *Geochim. Cosmochim. Acta*, 1996, **60**, 3023–3038.

73 Y. Joly, D. Cabaret, H. Renevier and C. R. Natoli, *Phys. Rev. Lett.*, 1999, **82**, 2398–2401.

74 L. X. Chen, T. Rajh, Z. Y. Wang and M. C. Thurnauer, *J. Phys. Chem. B*, 1997, **101**, 10688–10697.

75 G. Croft and M. J. Fuller, *Nature*, 1977, **269**, 585–586.

76 Y. Kuwahara, T. Ohmichi, K. Mori, I. Katayama and H. Yamashita, *J. Mater. Sci.*, 2008, **43**, 2407–2410.

77 R. Bouchet, A. Weibel, P. Knauth, G. Mountjoy and A. V. Chadwick, *Chem. Mater.*, 2003, **15**, 4996–5002.

78 K. Mori, H. Yamashita and M. Anpo, *RSC Adv.*, 2012, **2**, 3165–3172.